Nanoscale

ROYAL SOCIETY OF CHEMISTRY

PAPER

View Article Online
View Journal | View Issue

Cite this: *Nanoscale*, 2021, **13**, 13835

The screening of drug-induced nephrotoxicity using gold nanocluster-based ratiometric fluorescent probes†

Qin Liu,[a] Junyao Li,[a] Xiao Liu,[b] Lin Yuan,[b] Lingzhi Zhao,[a] Young-Tae Chang,[c] Xiaogang Liu[d] and Juanjuan Peng*[a]

Received 15th February 2021,
Accepted 1st July 2021

DOI: 10.1039/d1nr01006a

rsc.li/nanoscale

Herbal medicines are potential candidates for the treatment of various diseases, but their medication safety remains poorly regulated. Current screening methods for the herbal medicine-induced nephrotoxic effects include histological and serological assessments, which often fail to reflect the kidney dysfunction instantly. Here we report a ratiometric fluorescence approach for the rapid and facile screening of drug-induced acute kidney injury using chromophore-modified gold nanoclusters. These gold nanoclusters are highly sensitive to reactive oxygen species (ROS), with a detection limit of 14 nM for $^{\bullet}$OH. After passing through the glomerular filtration barrier, the gold nanocluster-based probes can quantify the fluctuation of the ROS level in the kidneys and evaluate the risk of drug-induced nephrotoxicity. We further employed nephrotoxic triptolide as the model drug and the screening of drug-induced early renal injury was demonstrated using the nanoprobes, which is unattainable by conventional diagnostic approaches. Our fluorescent probes also allow the identification of other nephrotoxic components from herbal medicine such as aristolochine, providing a high-throughput strategy for the screening of herbal supplement-induced nephrotoxicity.

Introduction

With the growing clinical practice of herbal medicine, increasing attention has been paid to its safety problem. Herbal medicine may consist of ingredients with severe renal and hepatic toxicity.[1,2] Kidneys are considered as one of the main metabolic organs, and are highly vulnerable because the renal blood flow delivers one-fourth of the cardiac output to the kidneys.[3] Drug-induced kidney injury (DIKI) accounts for 19–26% of acute renal failure,[4] causing over 2 million deaths per year globally.[5] Conventional DIKI screening approaches measure the serum creatinine (SCr) and blood urea nitrogen (BUN) levels from animals administered with the targeted compound.[6,7] Nevertheless, variations in these serological indicators usually lag behind the renal injury and thus fail to provide a facile and instant assessment of nephrotoxicity. Histopathological examination has been the gold standard for nephrotoxicity screening.[8] However, the diagnosis procedure is time-consuming and requires professional operators.[9] Therefore, it is critical to develop a convenient, rapid, and accurate screening method to identify the nephrotoxic components in herbal medicine.

Triptolide (TPL) is the active component of traditional Chinese herbal medicine Thunder God Vine (tripterygium wilfordiiHook F, TwHF), which has shown many therapeutic functions, such as immune regulation, anti-inflammatory activity,[10] anti-cancer activity[11] and contraceptive effect.[12] However, a high dose of TPL leads to kidney dysfunction and chronic kidney failure.[13] One of the main pathogenic factors of TPL is attributed to the burst of reactive oxygen species (ROS), such as hydroxyl radicals ($^{\bullet}$OH) and peroxynitrite ($ONOO^{-}$).[14] An excessive cellular level of ROS could cause oxidation to biomacromolecules, which can trigger the programmed cell death.[15,16] Thus, ROS is proposed as an early biomarker of kidney injury and a direct indicator of DIKI. However, it is challenging to monitor the *in situ* concentration of ROS in the living organism due to their short life-time. As a typical ROS generated in DIKI, $^{\bullet}$OH has a short life-time down to 1 ns,[17] which brings trouble for the determination of its level in kidneys by post-processing methods.

Fluorescence imaging has been widely applied to achieve sensitive, non-invasive, and real-time tracking of various bioanalytes in living organisms.[18–20] Many fluorescent probes

[a]*State Key Laboratory of Natural Medicine, the School of Basic Medical Sciences and Clinical Pharmacy, China Pharmaceutical University, Nanjing, Jiangsu 211198, China. E-mail: pjj@cpu.edu.cn*
[b]*State Key Laboratory of Chemo/Biosensing and Chemometrics, College of Chemistry and Chemical Engineering, Hunan University, Changsha 410082, Hunan, PR China*
[c]*Department of Chemistry, Pohang University of Science and Technology, Pohang, Gyeongbuk 37673, Korea*
[d]*Department of Chemistry, National University of Singapore, 117543, Singapore*
†Electronic supplementary information (ESI) available. See DOI: 10.1039/d1nr01006a

have been developed to monitor the expression of various biomarkers in living cells and tissues.[21,22] Fluorescent nanoparticles such as nanoclusters,[23–26] AIEgens,[27] semiconductor quantum dots,[28] upconversion nanoparticles[29] and carbon dots[30] have exhibited excellent optical properties to serve as fluorescent probes for biosensing and bioimaging applications. Among them, fluorescent gold nanoclusters (AuNCs) are regarded as one of the preferred materials due to their good optical performance, high stability and biocompatibility, which can be prepared using thiolate ligands such as glutathione (GSH).[31,32] It has been revealed that the luminescence of the AuNCs is generated by the aggregation induced emission effect of the staple-like Au(I)-thiolate motifs on the surface of the Au(0) core of the nanocluster.[33,34]

The interactions between the engineered nanoparticles and a variety of physiological barriers are highly dependent on the particle size. In the kidneys, larger nanoparticles are blocked by the glomerular filtration barrier, and only the nanoparticles with sizes below 6 nm can pass through the filter and be excreted with the urine.[35] To detect the endogenous ROS in the kidneys, the probe should be renal clearable after systematic administration. To this end, a probe with a very small size is required to infiltrate the fenestrated endothelium of the glomerular capillary. Therefore, the 2 nm GSH-protected AuNCs with outstanding optical performance, high stability, and low toxicity are ideal bioimaging agents to monitor the renal function.[31,36] These nanoclusters can enter the kidneys due to their smaller size than the filtration threshold.[31,37] On the other hand, the fluorescence of AuNCs can be quenched by ROS due to the oxidation for both the Au sites and GSH sites,[38] such as $^{\bullet}OH$ and $ONOO^{-}$, and can also be recovered by the addition of reductants such as ascorbic acid (AA).[39,40] Hence, AuNCs can be engineered as reversible fluorescent probes for the *in situ* detection of nephrotoxicity.

Until now, a few "turn-on" fluorescent probes for the detection of nephrotoxicity have been reported through the monitoring of ROS in kidneys.[41] Compared with "turn-on" or "turn-off" fluorescent probes with single-emission peaks, the two-channel ratiometric fluorescent probes possess higher sensitivity owing to their self-calibration characteristics, which effectively mitigates the interference from the complicated biological environment.[42]

In this work, a ratiometric and reversible fluorescent sensing system based on AuNCs was designed to screen the nephrotoxins (Scheme 1). We first synthesized ROS-responsive AuNCs with an emission peak at 600 nm. A stable fluorophore,

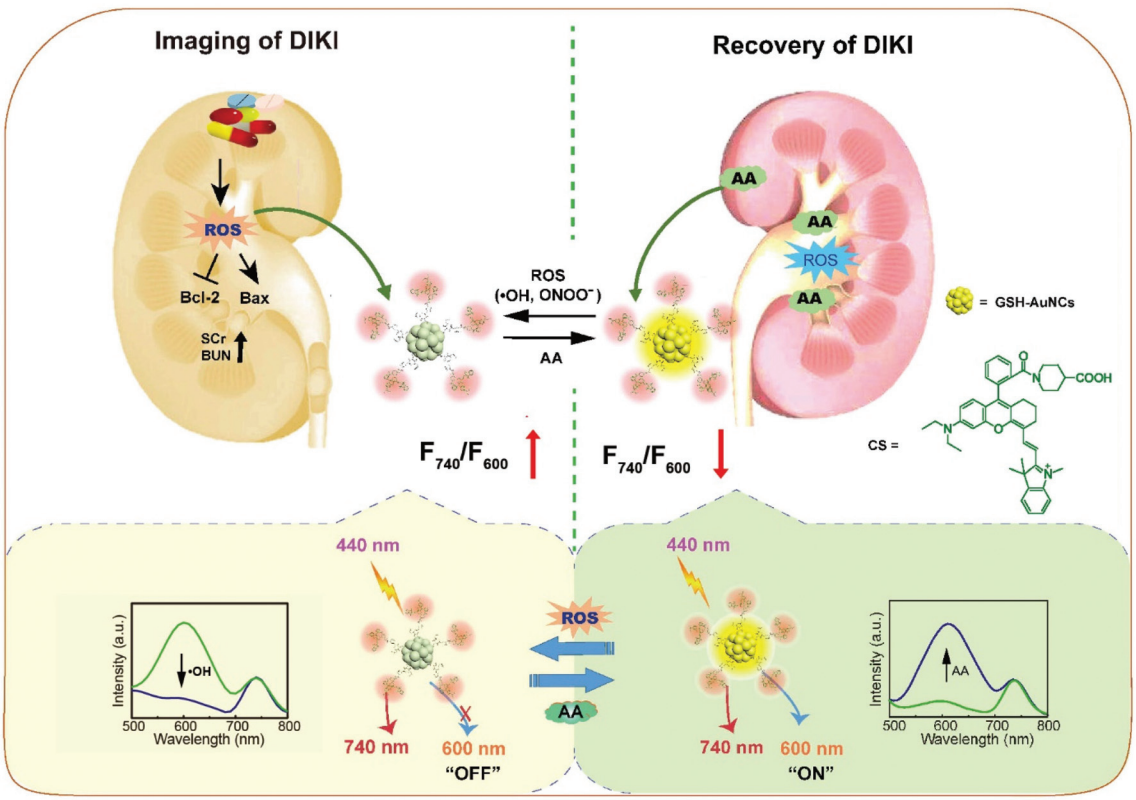

Scheme 1 The schematic diagram for the screening and therapy of the drug-induced kidney injury (DIKI). The AuNC-based nanoprobes are highly sensitive to ROS ($^{\bullet}OH$ or $ONOO^{-}$). The ratio of the fluorescence intensity at 740 nm (F_{740}) to the fluorescence intensity at 600 nm (F_{600}) increases in the presence of ROS. As excessive ROS can be an early biomarker of DIKI, the imaging of ROS can serve as a convenient tool for the diagnosis of DIKI. In addition, the sanitization of the ROS by the antioxidant AA can also be achieved by the recovery of the fluorescence, which enables the monitoring of the relief of DIKI.

Changsha (CS), with a stable emission peak at 740 nm was prepared and conjugated to the AuNCs as an internal reference. After intravenous injection, the nanoprobes can accumulate in the kidneys of the mouse and respond to the ROS (˙OH or $ONOO^-$). The emission of AuNCs at 600 nm decreased while the emission of the CS at 740 nm remained the same. Drug-induced nephrotoxins were screened by monitoring the ROS level in kidneys. The emission of AuNCs could be recovered after the injection of AA, enabling the monitoring of the renal rehabilitation. Finally, we demonstrated that the system is capable of screening the nephrotoxic components in herbal medicine *in vivo*.

Results and discussion

Design and synthesis of reversible and ratiometric fluorescent probes for ROS and AA monitoring

The AuNCs were synthesized using GSH as the ligand *via* a one-pot chemical reduction.[39] The obtained AuNCs are spherical nanoparticles (Fig. 1a) with an average diameter of 2.1 nm (Fig. S1†). The emission of the AuNCs peaked at 600 nm under 440 nm excitation (Fig. 1b), which is stable in both buffer solution and biological fluids (Fig. S2†). The optical properties of AuNCs in the presence of different kinds of ROS (such as H_2O_2, $O_2^{\bullet-}$, ˙OH and $ONOO^-$) were investigated. The fluorescence intensity of AuNCs decreased linearly with increasing concentrations of ˙OH and $ONOO^-$, respectively (Fig. 1b and Fig. S3†). The stability of the internal reference is crucial for the ratiometric probes. The CS dye, which has been proved stable to ROS,[43] was chosen as the internal reference for the ratiometric probes.[44] The CS molecules were modified with piperidine acid and conjugated to the GSH ligands on the surface of AuNCs (Scheme 1). Upon the addition of different types of ROS, the fluorescence intensity of the CS molecules remained almost constant at 740 nm (Fig. S4†), revealing their good stability in oxidative stress. The CS molecules were conjugated to the AuNCs through an amidation reaction.[24] Fourier transform infrared (FTIR) spectra confirmed the successful modification of the CS to AuNCs (Fig. S5†). The modification rate was determined as 8.14 μM CS on 1 mg mL^{-1} AuNCs (Fig. S6†). The TEM images showed that the CS-conjugation did not induce significant changes to the size and morphology of the AuNCs (Fig. S7†). Under the excitation at 440 nm, the nanoprobes displayed two well-resolved fluorescence peaks at 600 and 740 nm, which can be attributed to the emission of the AuNCs and the CS, respectively, which can be used for the ratiometric detection.

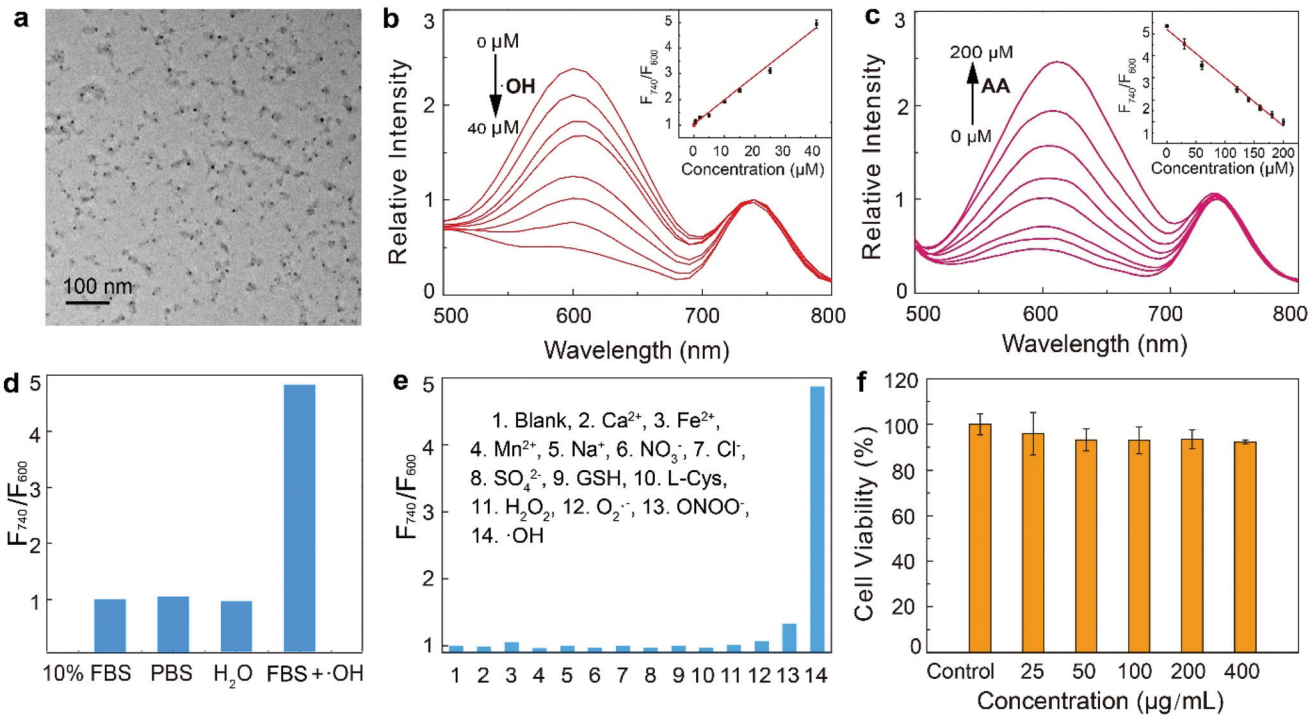

Fig. 1 The characterization of the nanoprobes. (a) The TEM imaging of AuNCs. (b) The fluorescence spectra of the CS-modified AuNCs recorded with different concentrations of ˙OH (0.5, 2, 5, 10, 15, 25 and 40 μM, λ_{ex} = 440 nm). Inset: The linear calibration of the fluorescence intensities *versus* ˙OH concentrations (c) The fluorescence spectra of the CS-modified AuNCs in the presence of 40 μM ˙OH and different concentrations of AA (0–200 μM). Inset: The linear calibration of the fluorescence intensities *versus* AA concentrations. (d) The stability of CS-modified AuNCs dispersed in different media for 24 h. (e) The selectivity assay of CS-modified AuNCs for different analytes: 1, blank; 2, Ca^{2+} (1 mM); 3, Fe^{2+} (1 mM); 4, Mn^{2+} (1 mM); 5, Na^+ (1 mM); 6, NO_3^- (1 mM); 7, Cl^- (1 mM), 8, SO_4^{2-} (1 mM); 9, GSH (1 mM); 10, L-Cys (1 mM); 11, H_2O_2 (200 μM); 12, O_2^- (200 μM); 13, $ONOO^-$ (20 μM); 14, ˙OH (40 μM). (f) The *in vitro* cell viability of HeLa cells incubated at 37 °C for 24 h with the nanoprobes of different concentrations.

ROS-Sensing of CS-modified AuNCs

As a proof-of-concept, the response of CS-modified AuNCs to ROS ($^{\bullet}OH$ and $ONOO^-$) was investigated in aqueous solution. With increasing concentrations of $^{\bullet}OH$, the fluorescence intensities at 600 nm decreased proportionally with the $^{\bullet}OH$ concentration, and the fluorescence of CS remained constant (Fig. 1b). The highest quenching efficiency of the 600 nm fluorescence is 77%, with 40 μM of $^{\bullet}OH$ added. The ratio of the fluorescence intensities at 740 nm and 600 nm also exhibited a good linear relationship with the concentration of $^{\bullet}OH$ (inset of Fig. 1b). The nanoprobe has a detection limit to $^{\bullet}OH$ of 14 nM, with a linear range of 0.5–40 μM, which is comparable to that for the reported probes for $^{\bullet}OH$ (Table S1†). Although the AuNCs can also be quenched by another ROS $ONOO^-$, the quenching efficiency is only limited to 21% (Fig. S8†). Therefore, in the bioimaging application, the nanoprobes are mainly responsive to $^{\bullet}OH$. By further adding AA to the $^{\bullet}OH$ treated nanoprobes, the fluorescence at 600 nm can be fully recovered (Fig. 1c). The stability of the probes was studied by dispersing the nanoprobes in different solutions (H_2O, PBS, and 10% FBS), and the fluorescence remained constant. In addition, the response of the nanoprobes to $^{\bullet}OH$ was not affected even after 24 h of incubation in the FBS, indicating that the developed nanoprobes are stable in biological environment. For selectivity assay, a series of solutions containing various biological ions (Ca^{2+}, Fe^{2+}, Mn^{2+}, Na^+, NO_3^-, Cl^-, SO_4^{2-}), thiol-bearing biomolecules (L-cysteine (L-Cys), GSH) and ROS (H_2O_2, O_2^-, $ONOO^-$, $^{\bullet}OH$) were employed for the test. The ions and biomolecules did not result in any change of the fluorescence (Fig. 1e). For the ROS, only $^{\bullet}OH$ and $ONOO^-$ induced attenuation of the fluorescence, and the responsiveness of the nanoprobes to $^{\bullet}OH$ was better than that of $ONOO^-$, revealing good selectivity of our nanoprobes to the target ROS. The biocompatibility of the nanoprobes was evaluated with methyl thiazolyl tetrazolium assay (MTT). After incubation with the nanoprobes of different concentrations for 24 h, the cell viabilities were all higher than 90% (Fig. 1f). All these results suggest that the nanoprobes can work as an ideal ratiometric sensor for the *in vivo* application.

Imaging of TPL-induced renal injury and remediation

Ultra-small AuNCs can be renally cleared and excreted through the kidneys (Fig. S9†). The biodistribution of the nanoprobes *in vivo* was studied by intravenous administration (1 mg mL^{-1}, 100 μL) to mice and their time-course biodistribution was traced by the fluorescence of both the AuCNs and CS (Fig. S10†). The results showed that the kidneys exhibited strong fluorescence signals, which peaked at 30 min and gradually declined after the injection (Fig. S10†). Therefore, the mice injected with the nanoprobes were sacrificed after 30 min postinjection in the following sensing applications to provide the best imaging quality. It is noteworthy that the F_{740}/F_{600} values almost remained constant during the 60 min (Fig. S10d†), implying that the signal of our ratiometric sensor is not affected by its concentration and locating position in the kidneys. According to the report, hypochlorite (ClO^-) can also affect the fluorescence of AuNCs.[39] However, endogenous ClO^- is produced by the myeloperoxidase, which is mostly present in neutrophils and monocytes.[45] In the early stage of the acute kidney injury, the primarily damaged cells are mainly renal tubular cells. The influx of neutrophils to the damaged kidneys takes 24 h to reach the peak,[46] and the recruitment of monocytes is behind the neutrophils.[47] Our probe can monitor the ROS in kidneys 30 min after the DIKI, in which the transmigration of neutrophils and monocytes has not yet taken place. Therefore, it can be inferred that the responsiveness to ClO^- could not affect the detection.

The *in vivo* biocompatibility of the nanoprobes was also tested. After intravenous administration of the nanoprobes (1 mg mL^{-1}, 100 μL) for 24 h, the mice were sacrificed and the tissues were collected for histological analysis. Mice injected with 100 μL of saline were used as the control. The hematoxylin–eosin (H&E) staining of the main organs (heart, liver, spleen, lungs and kidneys) showed that these probes induced no inflammation, lesions or cellular apoptosis, confirming the good biocompatibility of the CS-modified AuNCs (Fig. S11†).

The overdose of TPL can cause kidney injury due to the generation of excessive ROS. Hence, TPL was an ideal model drug to establish animal models of DIKI. To verify the capability of the nanoprobes, mice were intraperitoneally injected with TPL at different concentrations (0, 0.5 or 1 mg kg^{-1}) for 15 min, 30 min, 60 min and 48 h. The mice were then intravenously injected with the nanoprobes (100 μL, 1 mg mL^{-1}) and sacrificed at 30 min postinjection. The kidneys were collected for the fluorescence imaging. The fluorescence signals of AuNCs from TPL-treated mice decreased remarkably, and the CS emissions were similar compared with the control group (Fig. 2a), resulting in an increase of the F_{740}/F_{600} value. In addition, as the renal injury amplified along with more dosage and exposure time of TPL, the F_{740}/F_{600} values were found to be dependent on the dosage (0 mg kg^{-1}, 0.5 mg kg^{-1}, 1 mg kg^{-1}) and the administration period (15 min, 30 min, 60 min) of TPL, indicating that our probes can also reflect the degree of kidney injury. On the other hand, when the mice were treated with TPL for 48 h, the F_{740}/F_{600} values were reduced, which is probably due to the recession of the ROS level after its burst in the first few hours. According to the reports, some antioxidants, such as AA[48] or *N*-acetyl-L-cysteine (NAC),[49] can neutralize the free radicals and recover the TPL-induced oxidative stress in the kidneys. To demonstrate that the fluorescent probes can also indicate the recovery of DIKI, mice were pre-treated with AA (100 mg kg^{-1}) and then injected with TPL (1 mg kg^{-1}) for different periods (15, 30 and 60 min), followed by the administration of the nanoprobes. The F_{740}/F_{600} values of the kidneys with AA protection dramatically decreased compared with the AA-absent groups (Fig. 2b), confirming that the fluctuation of the ROS level in the kidneys can be monitored using the reversible nanoprobes.

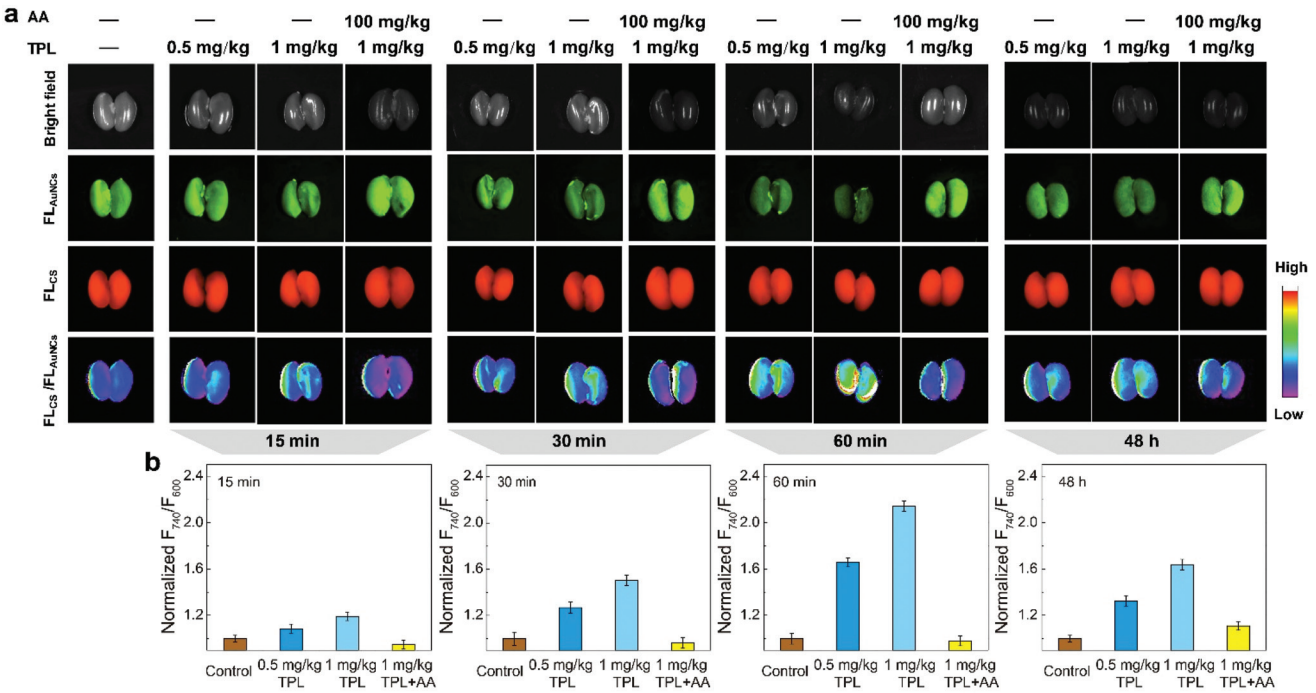

Fig. 2 The fluorescence imaging of TPL-induced renal injury of mice injected with the nanoprobes. (a) The representative images of the kidneys of the mice intravenously injected with the nanoprobes (1 mg mL^{-1}, 100 μL) after 30 min. Before the injection, the mice were pre-treated with saline, TPL (0.5 mg kg^{-1}, 1 mg kg^{-1}, intraperitoneally), or AA (100 mg kg^{-1}, intraperitoneally) for different periods. The fluorescence of AuNCs at 600 ± 20 nm and CS at 740 ± 20 nm was collected respectively (n = 3). (b) Normalized fluorescence intensity of the kidneys from each group of mice.

Conventional screening methods for the nephrotoxins include histopathological examination, serological analysis, and the analysis of the expression of marker protein. Those conventional methods were performed to benchmark our approach and verify the TPL-induced kidney injury. The histopathology images of hematoxylin and eosin (H&E) stained kidney sections show that severe damage such as detachment of tubular epithelial cells, necrosis of tubular epithelial cells, and tubular obstruction can only be found from the kidney tissue after a TPL-treatment period as long as 48 h (Fig. 3a, marked with a black arrow). However, in contrast to the bioimaging results, no discernible abnormality can be observed from the mice treated with TPL for 60 min for neither high (1 mg kg^{-1}) nor low administration dosage (0.5 mg kg^{-1}) of TPL. This implies that the burst of ROS occurs in the very early stage of kidney injury. Our probes can detect the DIKI and further screen the nephrotoxins not only more conveniently but also much earlier than the conventional histopathological methods.

Excessive ROS can inflict damage to biomolecules such as proteins and DNA, resulting in the death of the renal cells. The TdT-mediated dUTP nick-end labeling (TUNEL) assay was carried out to detect the apoptotic cells in the kidneys. Similar with the histopathological results, the TUNEL-positive cells (marked with white arrows) were not observed at 60 min but appeared at 48 h after TPL treatment. The expression of apoptosis-associated proteins Bcl-2 and Bax showed the same trend (Fig. 3c). The ratio of the pro-apoptotic protein Bax to the anti-apoptotic protein Bcl-2 remained the same after 1 h of TPL treatment and then upregulated after 48 h, confirming that the massive cellular apoptosis occurred far behind the ROS burst. As the fundamental renal function indicators, the concentrations of the SCr and BUN were tested.[50] The results (Fig. 3c) showed that both the SCr and BUN remained at normal levels for mice administered with TPL for 1 h either with high (1 mg kg^{-1}) or low (0.5 mg kg^{-1}) dosage. A significant rise of the two indicators was found only after 48 h. This result is in agreement with the clinical conclusion that the rise of SCr and BUN levels in blood lags behind the renal injury.[51] Therefore, our fluorescence approach is possible to diagnosis the DIKI by monitoring the oxidative stress before the physiological disorders of the kidney take place.

Screening of potential nephrotoxins

Inspired by the results of CS-modified AuNCs for TPL-induced kidney injury detection, the nanoprobes were utilized to screen the nephrotoxins from natural herbal medicines. Some components of natural medicines such as aristolochic acid,[52] tanshinone IIA[53] and geniposidic acid[54] were chosen as the model drugs. Cisplatin, a common chemotherapeutic drug,[55] with severe nephrotoxicity accompanied by the generation of endogenous ROS,[56] was used as a positive control. The mice were intraperitoneally injected with PBS or one of the drugs

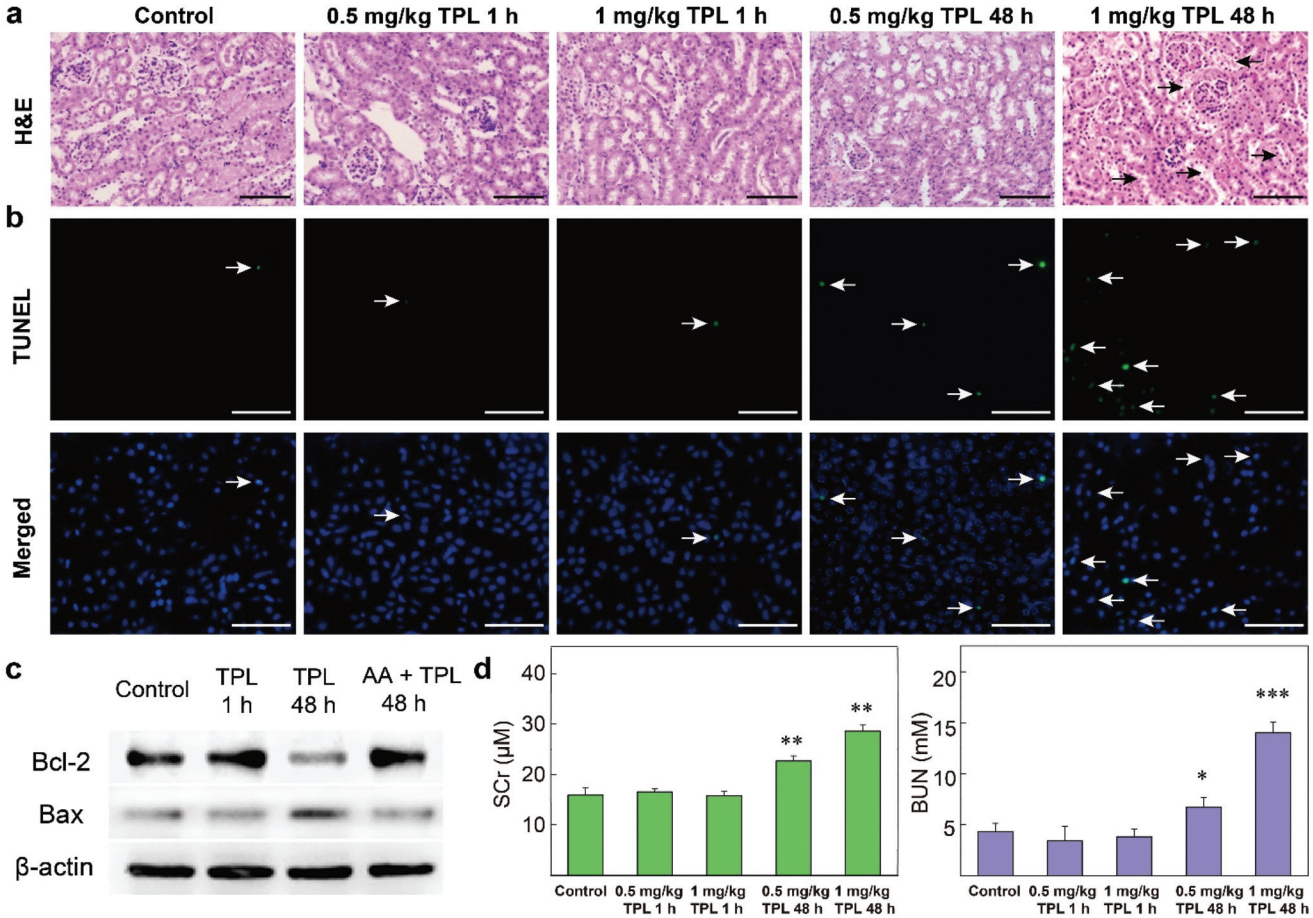

Fig. 3 The histopathological and serological analysis results of the mice with DIKI. (a) The representative H&E staining images of the kidneys from mice subjected to different treatments. Scale bars are 20 μm. (b) The cellular apoptosis analysis by TUNEL staining (green) to detect renal tissue damage from kidney sections from mice subjected to different treatments. The tissue sections were counterstained with DAPI (blue). Scale bars are 10 μm. (c) The serological analysis of SCr and BUN in serum (n = 6, mean ± SD). * $p < 0.05$, ** $p < 0.01$, *** $p < 0.005$, of different groups of mice. (d) The western blot analysis results of apoptosis-associated proteins Bcl-2 and Bax of the kidney.

for 1 h, followed by an intravenous injection of the nanoprobes. After 30 min, the kidneys of the mice were harvested for bioimaging (Fig. 4a). The fluorescence imaging data showed that the cisplatin or aristolochic acid-treated mice exhibited a distinct increase of the F_{740}/F_{600} value. In contrast, the tanshinone IIA- or geniposidic acid-treated groups remained virtually constant (Fig. 4b). These results indicate that the tanshinone IIA and geniposidic acid have no apparent nephrotoxicity, and the aristolochic acid generates endogenous ROS and causes severe renal lesions as with the positive control cisplatin, which is consistent with the notion that aristolochic acids from *Aristolochia* plants can lead to renal failure.[57] Moreover, the fluorescence imaging results indicate that one of the underlying pathogenic factors for aristolochic acid-induced kidney diseases is the ROS burst. Similar to the histopathological results obtained by TPL (Fig. 3a), the H&E-stained kidney sections showed no obvious damage from the kidney tissue 1 h after the administration of the cisplatin and aristolochic acid (Fig. 4c). Taken together, these data suggest that our nanoprobes can facilitate the early diagnosis of toxin-induced kidney injury, and enable the monitoring of disease progression, which may potentially offer timely decisions for patient management.

Experimental

Materials

Chemicals 2-(4-diethylamino-2-hydroxybenzoyl) benzoic acid, HATU, 1,3,3-trimethyl-2-(formylmethylene) indoline, cyclohexanone, isonipecotic acid, HATU, acetic anhydride, hydrogen peroxide (H_2O_2), sodium hypochlorite (NaClO), ferrous chloride, chloroauric acid ($HAuCl_4{\cdot}4H_2O$), 1-ethyl-3-(3-dimethylaminopropyl)carbodiimide hydrochloride (EDC), KO_2, and GSH were purchased from Sigma-Aldrich. All chemicals were of analytical reagent grade and used as received without further purification. The human cervical tumor cell line (HeLa) was purchased from ATTC. Dulbecco's modified Eagle's medium (DMEM medium) and fetal bovine serum (FBS) were supplied by Gibco. Antibodies against β-actin, Bax, and Bcl-2

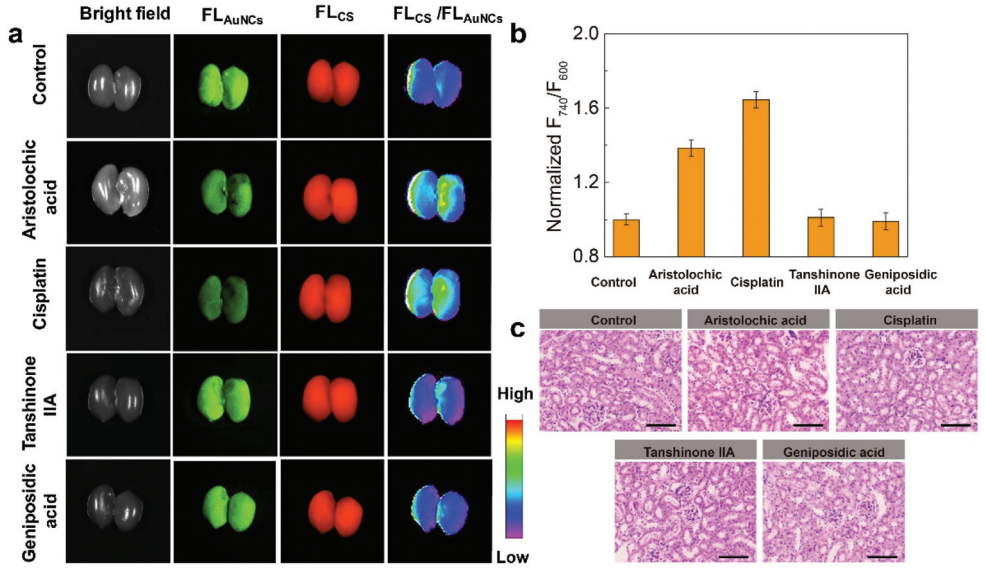

Fig. 4 The screening of the nephrotoxins using the fluorescent probes. (a) The bioimaging of the mouse kidneys intraperitoneally injected with saline, aristolochine (50 mg kg^{-1}), cisplatin (20 mg kg^{-1}), tanshinone IIA (4 mg kg^{-1}) or geniposidic acid (25 mg kg^{-1}) for 1 h, followed by intravenous injection of the nanoprobes. (b) The normalized fluorescence intensities from the kidneys treated with different drugs (n = 3). (c) The H&E staining images of kidney sections from mice treated with different drugs.

were obtained from Proteintech Group Inc. Male mice (4 weeks, 18–20 g) were purchased from Qinglongshan animal farm. All experimental animal procedures were in accordance with the Guide for the Care and Use of Laboratory Animals and were performed according to the institutional ethical guidelines for animal experiments.

Characterization

^{1}H NMR (500 MHz) and mass spectra of CS were obtained using a Bruker AV-500 NMR spectrometer (Bruker Co., Germany) and a Waters Q-TOF micro, respectively. Fourier transform infrared spectroscopy was performed using a Bruker TENSOR 27 spectrometer. The morphologies of AuNCs and CS-modified AuNCs were characterized using a transmission electron microscope (TEM) on JEM-1400Plus with an operating voltage of 120 kV. All absorption and fluorescence spectra were recorded in a Spectramax M5 microplate reader (Molecular Devices, the USA). Slices stained with H&E and TUNEL were observed with an inverted microscope (Nikon Ts2). *In vivo* fluorescence imaging was performed using a Fusion FX imaging system (Vilber Fusion FX7, France).

Generation of ROS

$O_2^{\bullet-}$ stock solutions were prepared by directly diluting commercially available KO_2 in DMSO. $^{\bullet}OH$ was generated by the Fenton reaction between Fe^{2+} and H_2O_2 at a molar ratio of 1 : 10. H_2O_2 solutions were purchased from Sigma-Aldrich. Peroxynitrite ($ONOO^-$) solution was prepared by mixing H_2O_2 (0.7 M, 1.5 mL), HCl (0.6 M, 1.5 mL), sodium nitrite (0.6 M, 3 mL), and sodium hydroxide (1.5 M, 3 mL). The resulting solution was split into small aliquots and stored at a temperature below −18 °C. The concentration of $ONOO^-$ was determined by measuring the absorbance at 302 nm (C_{ONOO^-} = $Abs_{302\ nm}$/1.67 mM).

Synthesis of AuNCs

Freshly prepared GSH aqueous solution (6 mM, 10 mL) and $HAuCl_4$ aqueous solution (4 mM, 10 mL) were added into a 50 mL round-bottom flask, followed by vigorous stirring at 90 °C for 6.5 h. The resulting yellow solutions were collected and centrifuged at 12 000 rpm for 10 min to remove large particles. The upper solution was transferred to a dialysis bag (1000 molecular weight cutoff) to remove unreacted species. Finally, AuNC solution was stored at 4 °C.[39]

Synthesis of compound 1

Compound **1** was synthesized by the reported method. Briefly, cyclohexanone (6.6 mL) and 2-(4-diethylamino-2-hydroxybenzoyl) benzoic acid were slowly added to 70 mL concentrated H_2SO_4 at 0 °C. Then, the mixture was heated at 90 °C for 1.5 h with vigorous stirring. After being cooled at room temperature, the resulting solution was poured into ice water with perchloric acid (7 mL) under stirring. The residue was washed with a large amount of ice water. Compound **1** was collected as a red solid and used directly for the next step (Scheme S1a†).

Synthesis of compound 2

Compound 1 (160 mg, 0.4 mM) and 1,3,3-trimethyl-2-(formylmethylene) indoline (88.5 mg, 0.44 mM) were added into a flask containing acetic anhydride (16 mL). The mixture was stirred at 50 °C for 30 min. Finally, water (16 mL) was poured into the above mixture to quench the reaction.[43] After cooling

to room temperature, the solvent was removed under vacuum, and the residue was purified by column chromatography on silica gel with (CH_2Cl_2/EtOH = 200 : 1 to 20 : 1), affording compound **2** as a green solid (Scheme S1b†).

Synthesis of compound CS

Compound **2**, isonipecotic acid and HATU were added into anhydrous dichloromethane (DCM). The above mixture was stirred under an N_2 flow at room temperature for 12 h.[41] After the reaction completed, the solvent was removed under vacuum, and the residue was purified by column chromatography on silica gel with (CH_2Cl_2/EtOH = 75 : 1) to yield CS as a solid (14.7 mg, 40.5%). (Scheme S1c†) MS (ESI) $C_{28}H_{15}N_4O_5$ $[M]^+$, found 670.43 (Fig. S12†) ^{1}H NMR (400 MHz, $CDCl_3$) δ 8.60 (d, J = 13.8 Hz, 1H), 7.64–7.56 (m, 2H), 7.49 (d, J = 6.7 Hz, 2H), 7.42 (d, J = 7.7 Hz, 1H), 7.28 (dd, J = 14.5, 7.1 Hz, 3H), 7.20 (d, J = 8.0 Hz, 1H), 6.85 (d, J = 9.0 Hz, 1H), 6.56 (s, 1H), 6.07 (d, J = 14.0 Hz, 1H), 3.68 (s, 4H), 3.54 (s, 4H), 2.73–2.51 (m, 4H), 2.38 (s, 1H), 1.94 (d, J = 12.5 Hz, 2H), 1.86 (s, 2H), 1.81 (s, 6H), 1.68–1.57 (m, 2H), 1.29 (s, 6H) (Fig. S13,† 14).

Preparation of the AuNC–CS conjugate

EDC (4.8 mg, 2.5 × 10^{-5} mol) and sulfo-NHS (2.9 mg, 2.5 × 10^{-5} mol) were added to dichloromethane containing CS (6.7 mL, 1 × 10^{-5} mol) with vigorously stirring for 4 h at room temperature. After addition of GSH-Au (2 mL, 20 mg mL^{-1}), the solution was stirred overnight at room temperature. The above mixture was placed in a dialysis bag (500 Da) for 24 h to remove the unreacted reagents.

Cytotoxicity of the as-prepared nanoprobes

In vitro cytotoxicity was measured using standard methyl thiazolyltetrazolium (MTT). HeLa cells were seeded at a density of 10 000 cells per well in 96-well plates and incubated for 24 h. The cells were further incubated with probes of different concentrations (0, 25, 50, 100, 200, and 400 μg mL^{-1}, diluted in DMEM) for 24 h. Methyl thiazolyl tetrazolium (20 μL, 5 mg mL^{-1}) was added into each well for an additional 4 h. Finally, the medium was removed, and 100 μL of DMSO was added into each well. The absorbance was measured at 490 nm using a SpectraMax M5 (Molecular Devices) plate reader.

Imaging of TPL-induced renal injury and remediation

All animal experiments were performed in accordance with the Guidelines for Care and Use of Laboratory Animals of China Pharmaceutical University and approved by the Animal Ethics Committee of School of Pharmacy, China Pharmaceutical University. The BALB/c mice (4–5 weeks old, male) were purchased from Qinglongshan animal center.

Mice were intraperitoneally injected with different concentrations of TPL (0, 0.5 mg kg^{-1}, 1 mg kg^{-1}) for different time periods (15 min, 30 min, 60 min, 48 h). CS-modified AuNCs (1 mg mL^{-1}) were then intravenously injected into the mice for 30 min. After 30 min, the mouse kidneys were collected for fluorescence imaging.

Before TPL injection, the male mice were intraperitoneally injected with AA (100 mg kg^{-1}) for different periods (15 min, 30 min, 60 min). The probes (1 mg mL^{-1}) were injected through the mouse tail vein one hour after TPL injection. As stated above, the kidneys were harvested for imaging.

Screening of the potential nephrotoxins

Mice were intraperitoneally injected with saline, aristolochic acid (50 mg kg^{-1}), cisplatin (20 mg kg^{-1}), tanshinone IIA (4 mg kg^{-1}) or geniposidic acid (25 mg kg^{-1}). The mice were injected with the probes (1 mg mL^{-1}, 100 μL) one hour after injection. After 30 min, the mice were anesthetized, and the kidneys were dissected for imaging.

Histopathological studies

Mice were injected with different concentrations of TPL for different periods and then sacrificed. The main organs were obtained for histopathological study. Fixed organ tissues were stained with hematoxylin and eosin according to a conventional method. And the morphology of any observed lesions was classified and recorded according to the classification criteria. Kidneys were homogenized and subjected to SDS/PAGE. Protein was quantified with a BCA protein assay kit. An equal amount of proteins was separated by SDS-PAGE (10%) and transferred to PVDF membranes. The membrane was blocked with 5% nonfat milk in PBST for three hours at room temperature and incubated with primate antibody against the target proteins overnight at 4 °C. After washing three times with PBST, appropriate HRP-conjugated secondary antibodies were used to quantify protein. The films were developed using an enhanced chemiluminescence (ECL) detection system.

Conclusions

In summary, we have developed ratiometric and reversible fluorescent probes by combining ROS-responsive AuNCs and ROS-stable fluorescent dye CS. The hybrid nanoprobes can pass through the kidneys and response to the elevated endogenous ROS. These nanoprobes were demonstrated as a convenient platform to monitor the DIKI in living mice and were able to rapidly screen the toxic components of the herbal medicines. Compared with the gold standard in clinical trials for the screening of nephrotoxicity, the ratiometric fluorescence method presents a distinct strategy to serve the early diagnosis of DIKI, which could help to improve the safety of the herbal medicine-related therapy.

Conflicts of interest

There are no conflicts to declare.

Acknowledgements

The authors gratefully acknowledge the financial support from the National Natural Science Foundation of China (81701766, 81971725 and 81702998), Postgraduate Research & Practice Innovation Program of Jiangsu Province (KYCX19_0686) and Six Talent Peaks Programme of Jiangsu Province (SWYY-104).

Notes and references

1 A. Popat, N. H. Shear, I. M. Malkiewicz, M. J. Stewart, V. Steenkamp, S. Thomson and M. G. Neuman, *Clin. Biochem.*, 2001, **34**, 229–236.
2 S. De and A. G. M. Peter, *Clin. Pharmacol. Ther.*, 2004, **76**, 1–17.
3 N. K. Hollenberg, D. F. Adams, H. S. Solomon, A. Rashid, H. L. Abrams and J. P. Merrill, *Circ. Res.*, 1974, **34**, 309–316.
4 H. Izzedine and M. A. Perazella, *Kidney Int. Rep.*, 2017, **2**, 504–514.
5 A. Linkermann, G. C. Chen, G. Dong, U. Kunzendorf, S. Krautwald and Z. Dong, *J. Am. Soc. Nephrol.*, 2014, **25**, 2689–2701.
6 C. L. Edelstein, *Adv. Chronic Kidney Dis.*, 2008, **15**, 222–234.
7 L. A. Stevens and A. S. Levey, *J. Am. Soc. Nephrol.*, 2009, **20**, 2305–2313.
8 L. V. Meer, M. Moerland, A. F. Cohen and J. Burggraaf, *Br. J. Clin. Pharmacol.*, 2014, **77**, 947–957.
9 E. Flores, O. Yelamos, M. Cordova, K. Kose, W. Phillips, E. H. Lee, A. M. Rossi, K. S. Nehal and M. Rajadhyaksha, *J. Eur. Acad. Dermatol. Venereol.*, 2019, **33**, 1084–1091.
10 B. J. Chen, *Leuk. Lymphoma*, 2001, **42**, 253–265.
11 Y. W. Chen, G. J. Lin, W. T. Chia, C. K. Lin, Y. P. Chuang and H. K. Sytwu, *Oral Oncol.*, 2009, **45**, 562–568.
12 C. E. Hoesl, F. Saad, M. Pöppel and J. E. Altwein, *Eur. Urol.*, 2005, **48**, 712–723.
13 X. X. Li, F. Y. Du, H. X. Liu, J. B. Ji and J. Xing, *J. Ethnopharmacol.*, 2015, **162**, 238–243.
14 X. Wang, R. Tian, Y. Yang, Z. Lu, X. Han, X. Liu, W. Mao, P. Xu, H. Xu and B. Liu, *Biomed. Pharmacother.*, 2019, **118**, 109232.
15 M. Valko, C. J. Rhodes, J. Moncol, M. Izakovic and M. Mazur, *Chem. – Biol. Interact.*, 2006, **160**, 1–40.
16 J. T. Coyle and P. S. Puttfarcken, *Science*, 1993, **262**, 689–695.
17 Z. Qianqian, Z. Daixin, Z. Song, C. Kong and J. lie, *ACS Appl. Mater. Interfaces*, 2017, **9**, 2052–2058.
18 H. Kobayashi, M. Ogawa, R. Alford, P. L. Choyke and Y. Urano, *Chem. Rev.*, 2010, **110**, 2620–2640.
19 J. G. Huang, J. C. Li, Y. Lyu, Q. Miao and K. Pu, *Nat. Mater.*, 2019, **18**, 1133–1143.
20 Y. Y. Jiang, J. G. Huang, X. Zhen, Z. Zeng, J. Li, C. Xie, Q. Miao, J. Chen, P. Chen and K. Pu, *Nat. Commun.*, 2019, **10**, 2064.
21 W. M. Ren, J. J. Zhang, C. Peng and H. j. Xiang, *Bioconjugate Chem.*, 2018, **29**, 3459–3466.
22 Z. Zhou, F. Wang, G. Yang, C. Lu, J. Nie, Z. Chen, J. Ren, Q. Sun, C. Zhao and W. Zhu, *Anal. Chem.*, 2017, **89**, 11576–11582.
23 R. Jin, C. Zeng, M. Zhou and Y. Chen, *Chem. Rev.*, 2016, **116**, 10346–10413.
24 I. Chakraborty and T. Pradeep, *Chem. Rev.*, 2017, **117**, 8208–8271.
25 Y. Xiao, Z. Wu, Q. Yao and J. Xie, *Aggregate*, 2021, **2**, 114–132.
26 Z. Liu, Z. Wu, Q. Yao, Y. Cao and J. Xie, *Nano Today*, 2021, **36**, 101053.
27 Y. C. Chiang, Z. L. Lai, C. M. Chen, C. C. Chang and B. Liu, *J. Mater. Chem. B*, 2018, **6**, 2869–2876.
28 Y. Ibrahim, T. Massimiliano and M. R. Franisco, *J. Mater. Chem. B*, 2008, **18**, 5577–5584.
29 L. Cheng, W. Chao and Z. Liu, *Nanoscale*, 2012, **5**, 23–37.
30 S. T. Yang, W. Xin, H. Wang, F. Lu and Y. P. Sun, *J. Phys. Chem. C*, 2009, **113**, 18110.
31 M. Yu, J. Xu and J. Zheng, *Angew. Chem., Int. Ed.*, 2019, **58**, 4112–4128.
32 Z. Luo, X. Yuan, Y. Yu, Q. Zhang, D. T. Leong, J. Y. Lee and J. Xie, *J. Am. Chem. Soc.*, 2012, **134**, 16662–16670.
33 Z. Wu, Q. Yao, S. Zang and J. Xie, *Natl. Sci. Rev.*, 2021, **8**, nwaa208.
34 Z. Wu, Q. Yao, O. Chai, N. Ding, W. Xu, S. Zang and J. Xie, *Angew. Chem., Int. Ed.*, 2020, **59**, 9934–9939.
35 B. J. Du, X. Y. Jiang, A. Das, Q. Zhou, M. Yu, R. Jin and J. Zheng, *Nat. Nanotechnol.*, 2017, **12**, 1096–1102.
36 M. Matulionyte, R. Marcinonyte and R. Rotomskis, *J. Biomed. Opt.*, 2015, **20**, 051018.
37 C. Q. Peng, J. Xu, M. X. Yu, X. Ning, Y. Huang, B. Du, E. Hernandez, P. Kapur, J. T. Hsieh and J. Zheng, *Angew. Chem., Int. Ed.*, 2019, **58**, 8479–8483.
38 Y. Xie, X. Yunlei, N. Wang, Z. Yan, Y. Liu, K. Zhu, N. Hatzakis and X. Jiang, *Adv. Funct. Mater.*, 2018, **28**, 1702026.
39 T. T. Chen, Y. H. Hu, Y. Cen, X. Chu and Y. Lu, *J. Am. Chem. Soc.*, 2013, **135**, 11595–11602.
40 L. Z. Hu, L. Deng, S. Alsaiari, D. Zhang and N. M. Khashab, *Anal. Chem.*, 2014, **86**, 4989–4994.
41 D. Cheng, J. J. Peng, Y. Lv, D. Su, D. Liu, M. Chen, L. Yuan and X. Zhang, *J. Am. Chem. Soc.*, 2019, **141**, 6352–6361.
42 K. Yin, F. B. Yu, W. W. Zhang and L. Chen, *Biosens. Bioelectron.*, 2015, **74**, 156–164.
43 L. Yuan, W. Lin, Y. Yang and H. Chen, *J. Am. Chem. Soc.*, 2012, **134**, 1200–1211.
44 J. J. Peng, A. Samanta, X. Zeng, S. Han and T. C. Young, *Angew. Chem., Int. Ed.*, 2017, **56**, 4165–4169.
45 C. C. Winterbourn, M. C. Vissers and A. J. Kettle, *Curr. Opin. Hematol.*, 2000, **7**, 53–58.
46 D. A. C. Messerer, R. Halbgebauer, B. Nilsson, H. Pavenstädt, P. Radermacher and M. Huber-Lang, *Nat. Rev. Nephrol.*, 2021, **17**, 91–111.
47 D. A. Ferenbach and J. V. Bonventre, *Nat. Rev. Nephrol.*, 2015, **11**, 264–276.

48 Y. Liu, H. Hong, X. Lu, W. Wang, F. Liu and H. Yang, *Biol. Trace Elem. Res.*, 2017, **175**, 428–439.
49 M. Halasi, M. Wang, T. S. Chavan, V. Gaponenko, N. Hay and A. L. Gartel, *Biochem. J.*, 2013, **454**, 201–208.
50 V. S. Vaidya, J. S. Ozer, F. Dieterle, F. B. Collings, V. Ramirez, S. Troth, N. Muniappa, D. Thudium, D. Gerhold and D. J. Holder, *Nat. Biotechnol.*, 2010, **28**, 478–485.
51 E. J. Weber, J. Himmelfarb and E. J. Kelly, *Curr. Opin. Toxicol.*, 2017, **4**, 16–21.
52 V. M. Arlt, M. Stiborova and H. H. Schmeiser, *Mutagenesis*, 2002, **17**, 265–277.
53 S. Gao, Z. Liu, H. Li, P. J. Little, P. Liu and S. Xu, *Atherosclerosis*, 2012, **220**, 3–10.
54 H. Hsu, J. Yang, S. Lin and C. Lin, *Cancer Lett.*, 1997, **113**, 31–37.
55 D. K. Armstrong, B. N. Bundy, L. Wenzel, H. Q. Huang, R. N. Baergen, S. Lele, L. J. Copeland, J. L. Walker and R. A. Burger, *N. Engl. J. Med.*, 2006, **354**, 34–43.
56 M. A. Dkhil, S. Alquraishy, A. M. Aref, M. S. Othman, K. M. Eldeib and A. E. A. Moneim, *Oxid. Med. Cell. Longevity*, 2013, **2013**, 741817–741817.
57 C. L. Cheng, K. J. Chen, P. Shih, L. Lu, C. Hung, W. Lin and J. Y. Gu, *Cancer Lett.*, 2006, **232**, 236–242.